PHOTONICS Research

Ultrafast modulable 2DEG Huygens metasurface

Hongxin Zeng,[1,2,†] Xuan Cong,[1,†] Shiqi Wang,[1] Sen Gong,[1,2] Lin Huang,[1] Lan Wang,[1,2]
Huajie Liang,[3] Feng Lan,[1,2] Haoyi Cao,[1] Zheng Wang,[1] Weipeng Wang,[1] Shixiong Liang,[4]
Zhihong Feng,[4] Ziqiang Yang,[1,2] Yaxin Zhang,[1,2,6] and Tie Jun Cui[2,5,7]

[1]Terahertz Communication Laboratory, School of Electronic Science and Engineering, University of Electronic Science and Technology
of China, Chengdu 611730, China
[2]Zhangjiang Laboratory, Shanghai 201210, China
[3]Yangtze Delta Region Institute (Huzhou), University of Electronic Science and Technology of China, Huzhou 313098, China
[4]National Key Laboratory of Solid-State Microwave Devices and Circuits, Hebei Semiconductor Research Institute, Shijiazhuang 050051, China
[5]Institute of Electromagnetic Space and State Key Laboratory of Millimeter Waves, Southeast University, Nanjing 210096, China
[6]e-mail: zhangyaxin@uestc.edu.cn
[7]e-mail: tjcui@seu.edu.cn
[†]These authors contributed equally to this work.

Huygens metasurfaces have demonstrated remarkable potential in perfect transmission and precise wavefront modulation through the synergistic integration of electric resonance and magnetic resonance. However, prevailing active or reconfigurable Huygens metasurfaces, based on all-optical systems, encounter formidable challenges associated with the intricate control of bulk dielectric using laser equipment and the presence of residual thermal effects, leading to limitations in continuous modulation speeds. Here, we present an ultrafast electrically driven terahertz Huygens metasurface that comprises an artificial microstructure layer featuring a two-dimensional electron gas (2DEG) provided by an AlGaN/GaN heterojunction, as well as a passive microstructure layer. Through precise manipulation of the carrier concentration within the 2DEG layer, we effectively govern the current distribution on the metasurfaces, inducing variations in electromagnetic resonance modes to modulate terahertz waves. This modulation mechanism achieves high efficiency and contrast for terahertz wave manipulation. Experimental investigations demonstrate continuous modulation capabilities of up to 6 GHz, a modulation efficiency of 90%, a transmission of 91%, and a remarkable relative operating bandwidth of 55.5%. These significant advancements substantially enhance the performance of terahertz metasurface modulators. Importantly, our work not only enables efficient amplitude modulation but also introduces an approach for the development of high-speed and efficient intelligent transmissive metasurfaces. © 2024 Chinese Laser Press

https://doi.org/10.1364/PRJ.517350

1. INTRODUCTION

Metasurfaces are sub-wavelength artificial electromagnetic structures capable of precisely controlling incident electromagnetic waves, including their amplitude, phase, polarization, and beam direction [1–3]. In recent years, extensive research has demonstrated various metasurfaces with specific functionalities, such as metalenses [4–7], beam deflectors [8–11], and polarization converters [12–14]. As digital information technology, artificial intelligence, and next-generation communication systems continue to advance, there is an increasing demand for metasurfaces capable of dynamically manipulating electromagnetic waves with high speed and efficiency [15–17]. Consequently, significant efforts have been devoted to integrating metasurfaces with tunable materials, enabling active control through electrical, optical, and temperature excitations. Examples include tunable absorbers [18–20], intelligent

reflective surfaces (IRSs) [21–24], phase modulators [25–27], amplitude modulators [28–30], tunable lenses [31–33], and digital metasurfaces [34–37]. However, these active metasurfaces primarily rely on the tuning of a single electrical resonance (ER), thereby hindering the reduction of insertion loss and limiting the realization of superior characteristics such as high transmittance, reflection suppression, and complete phase coverage.

Compared with single ER metasurfaces, the Huygens metasurface exhibits synchronous electrical magnetic resonance (EMR), and by adjusting the intensity of the ER-MR coupling, the insertion loss of the device can be significantly reduced, the transmission rate can be enhanced, and the electromagnetic wave can be manipulated more flexibly [38–40]. In the microwave band, the utilization of a multi-layer dynamic structure facilitates control over ER and MR, thereby forming Huygens metasurfaces [41,42]. However, as the operating

frequency increases, the reduction in wavelength poses challenges in achieving sub-wavelength scale bilayer dynamic structures on the substrate. Current active Huygens metasurfaces employ all-optical tunable all-dielectric strategies, such as doped silicon and germanium antimony telluride compounds, within the terahertz (THz) and optical frequency bands [43–47]. The prevailing optical excitation methods predominantly rely on pulse modulation techniques; while literature demonstrates the attainment of picosecond-level or even femtosecond-level response rates [48–54], challenges persist in sustaining long-term continuous wave modulation owing to the persistent thermal residual issues of the dielectric material, thereby constraining its utility in communication, imaging, and diverse domains. Urgent innovation is imperative to surmount the existing impediment of sluggish continuous response rates, necessitating the development of novel mechanisms for enhanced operational efficiency and expanded applicability. The two-dimensional electron gas (2DEG) based on AlGaN/GaN heterojunction [55] has high electron mobility and carrier concentration, which can provide a faster continuous modulation response, so combining it with a metal microstructure can achieve continuous high-speed modulation. However, the current metasurfaces based on GaN-HEMT [56–58] are all single-layer structures, and the operating mode is a single ER state, which limits the working bandwidth and transmission.

In this paper, we propose a double-layer metasurface structure combining GaN-2DEG and the Huygens principle, which can not only reduce insertion loss and enhance the transmission characteristics of metasurfaces, but also broaden the bandwidth and improve the modulation speed. As a demonstration, we present a high-speed dynamic amplitude control device for free space THz waves, achieving a monophonic 6 GHz modulation speed, 90% modulation efficiency, and 91% transmission. This

breakthrough not only surpasses the limitations of traditional multi-layer modulated dynamic Huygens metasurfaces but also addresses the issue of slow response speeds encountered with all-dielectric dynamic Huygens metasurfaces. Moreover, our approach provides a novel avenue for low-loss, high-efficiency, and high-speed THz dynamic manipulation, opening new possibilities in this field.

2. RESULTS AND DISCUSSION

A. Principle of the 2DEG Huygens Metasurface

The dynamic Huygens metasurface proposed is a sandwich structure comprising a double layer artificial microstructure and a dielectric substrate, as illustrated in Fig. 1. The metasurface has a total thickness of approximately 0.11λ (where λ represents the operation wavelength in free space). The top subunit of the metasurface consists of an I-shaped metal structure (IMS) embedded with a 2DEG provided by AlGaN/GaN HEMT (for detailed model information, refer to Section 4.A). Four subunits are connected in series to form a single top unit, and each row of HEMT is linked by a gate while sharing a common source and drain, thereby creating a gate-controlled 2DEG transistor array. Additionally, the bottom unit of the metasurface comprises two split resonant rings (SRRs) positioned beneath the IMS at both ends of the top unit. The 2DEG, serving as the pivotal structure for dynamically controlling the electron distribution of the metasurfaces, enables adjustment of the phase difference between the top and bottom surface currents by regulating its concentration. In its initial state, the 2DEGs are uniformly distributed, maintaining a high electron concentration. The THz wave-induced electrons smoothly traverse the entire top unit, generating long dipole ER, while the SRRs assume an in-phase ER state. These
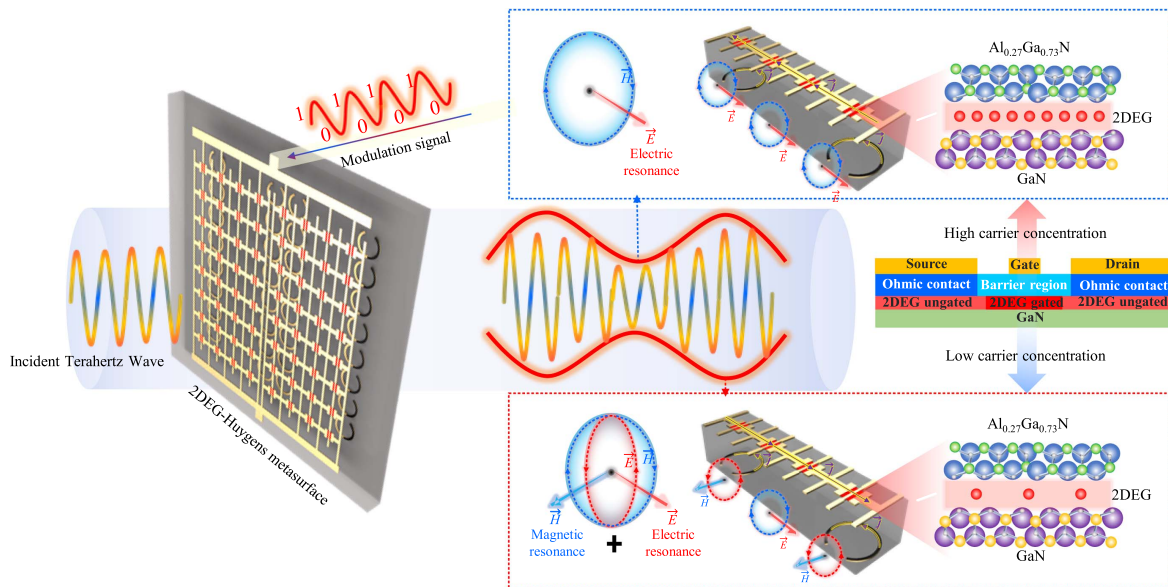

Fig. 1. Schematic diagram of the overall effect of Huygens metasurface. All metal layers are 50 nm thick gold, fabricated on both sides of 100 μm SiC substrates. 2DEG with a thickness of 3 nm is provided by AlGaN/GaN HEMT, which is composed of a GaN layer with a dielectric constant of 8.9 and a thickness of 1.5 μm, and an AlGaN layer of 25 nm. The carrier concentration at room temperature is 1.125×10^{13} cm^{-2}, electron mobility 2248 cm^2/(V·s), and square resistance 250.3 Ω/□. The applied gate voltage controls the carrier concentration of 2DEG and flexibly handles the current distribution of the top and bottom units on the metasurface.

two ER modes interact and merge, resulting in a unified pure ER mode that leads to the reflection of normally incident THz waves. Upon application of a gate voltage, the free electrons within the 2DEG are depleted, causing capacitive effects among the IMSs and leading to a phase delay between the top and bottom surface currents inducing an equivalent MR mode. Notably, there is no SRR below the two IMSs in the middle of the top unit and thus they remain in an ER state. In this configuration, the metasurface exhibits EMR, enabling high transmission of THz waves. Building upon this concept, when modulation signals are applied to the 2DEG transistor array in a Huygens metasurface, the transmission intensity of incident THz waves in free space can be modulated with exceptional speed and efficiency.

B. Operation of Huygens Resonance

Within a metasurface, individual units can be considered as Huygens sources comprising magnetic and electrical dipoles supported by both IMSs and SRRs. When a terahertz (THz) wave impinges upon the Huygens metasurface, it induces transverse electric and magnetic currents, which can be effectively described by the average surface impedance. Local boundary conditions for the incident wave can be defined in terms of the normalized surface magnetic impedance Z^e_{ms} and surface electric admittance Y^e_{es} (refer to Section 4.B for a comprehensive theoretical derivation), directly related to the complex reflection and transmission coefficients of the metasurface [59]. By varying the carrier concentration of nanostructured 2DEG, the distribution of magnetic and electric currents on

the Huygens metasurface can be dynamically adjusted, allowing flexible tuning of the real and imaginary parts of Z^e_{ms} and Y^e_{es}. It is known from previous theoretical knowledge that perfect transmission with no reflection occurs when the normalized surface admittance and impedance are equal and purely imaginary ($Y^e_{es} = Z^e_{ms}$) [60–62]. Employing the generalized boundary transformation condition, we calculate the real and imaginary components of Y^e_{es} and Z^e_{ms} for different carrier concentrations, resulting in near-perfect transmission at 333 GHz (refer to Section 4.B for detailed calculation methodology).

To elucidate the dynamic resonance process, CST Microwave Studio's frequency domain solver is employed to simulate and monitor the current and magnetic fields. Y-polarized THz waves are incident vertically onto the metasurface. In order to characterize the electron transport in the 2DEG, a Drude model is established (see Section 4.A for model details). Figure 2(a) illustrates the distribution of magnetic fields and current density on the Huygens metasurface with an initial carrier concentration of 10^{14} cm^{-2}. The 2DEG nanostructures are filled with free electrons, facilitating effective electrical connections between adjacent IMSs on the metasurface, inducing long dipole electric resonances. It can be observed that both top and bottom structures exhibit currents predominantly in the y direction. Furthermore, the surface current calculations indicate a phase difference of 20° between the top and bottom currents, as depicted by the blue solid line in Fig. 2(e). The opposing currents generate equivalent magnetic fields that counteract each other within the substrate, resulting in independent ER. As the carrier concentration decreases, the
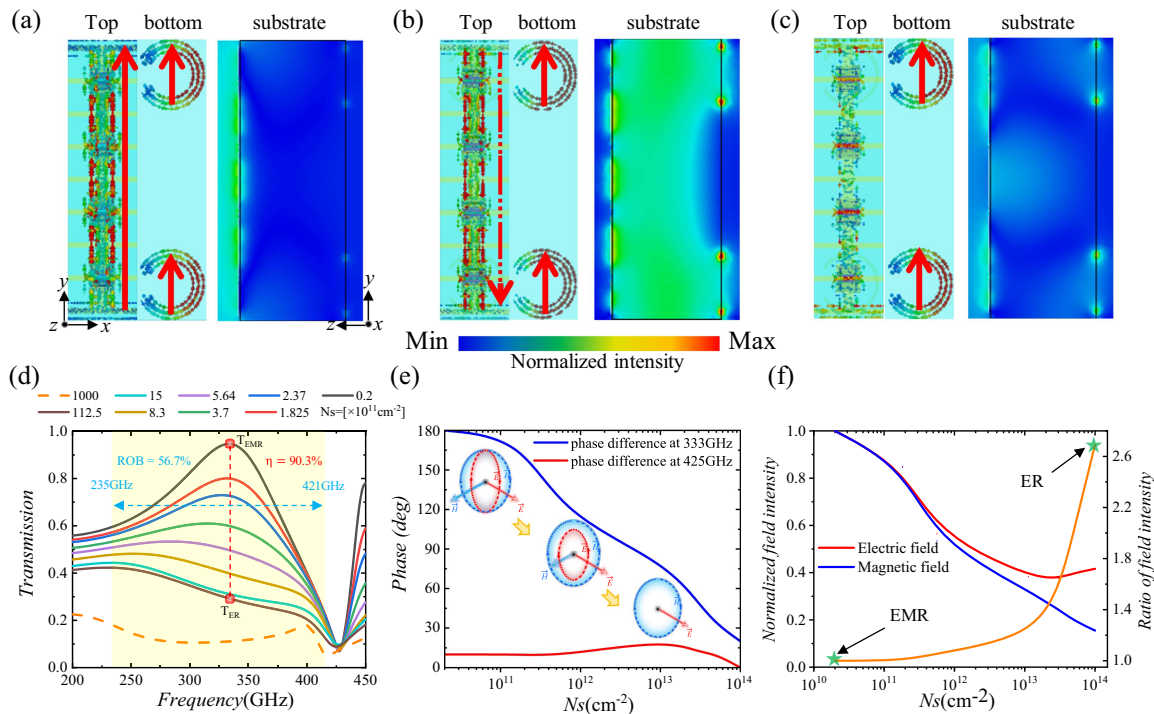

Fig. 2. Electromagnetic properties of the Huygens metasurface. (a)–(c) Magnetic field and surface current distribution at (a) 333 GHz with 10^{14} cm^{-2} carrier densities, (b) 333 GHz with 2×10^{10} cm^{-2} carrier densities, and (c) 425 GHz with 2×10^{10} cm^{-2} carrier densities. (d) Transmission spectra at different carrier concentrations. (e) Phase difference of the top and bottom current. (f) Normalized intensity of electric and magnetic fields at 333 GHz.

electron transport channels within the 2DEG nanostructure become increasingly constrained, leading to a pronounced capacitive effect between adjacent IMSs. This, in turn, causes a phase delay in the surface currents of the IMSs. Upon reducing the carrier concentration to 2×10^{10} cm^{-2}, the electron channels within the 2DEG nanostructure are fully depleted, giving rise to multiple independent short dipole electric resonances. In Fig. 2(b), the surface currents of the IMSs and SRRs at both ends flow in opposite directions along the y direction, while the phase difference between the currents amounts to 180° [refer to the blue solid line in Fig. 2(e)]. The equivalent magnetic fields produced by these currents are superimposed and enhanced within the substrate, resulting in independent MR. Notably, the two IMSs located in the middle of the top unit lack counterpart SRRs on the bottom unit, maintaining independent ER consistently. This suggests the existence of an EMR mode within the Huygens metasurface.

Figure 2(d) presents the transmission spectrum of the Huygens metasurface, showcasing the resonance mode transition from EMR to ER as the carrier concentration of the 2DEG gradually increases. Consequently, the THz propagation transmittance decreases from $T_{\text{EMR}} = 0.925$ to $T_{\text{ER}} = 0.115$. This resonance transition yields a remarkable 90.3% power modulation efficiency [$\eta = ((T_{\text{EMR}}^2 - R_{\text{ER}}^2)/T_{\text{EMR}}^2) \times 100\%$], and a half-efficiency frequency coverage spanning 235 to 421 GHz, with a relative operating bandwidth (ROB) of 56.7%. The underlying driving force behind the expanded operational bandwidth originates from a stationary resonance in proximity to the transition region, as exemplified in Fig. 2(c). At this specific frequency, THz waves weakly interact with IMSs, resulting in feeble surface currents. Conversely, these waves interact strongly with SRRs, inducing robust current and pronounced electric resonances. The aforementioned resonance synergizes with the resonance of the top unit featuring a high concentration of 2DEG, giving rise to a superposition of resonant frequencies, as visually represented by the yellow dotted line in Fig. 2(d). This superposition effect engenders an expanded modulation bandwidth, concomitant with diminished transmission spanning the entire spectral range. Due to the passive nature of the SRRs involved in this resonance, the phase of the surface current remains relatively unchanged, irrespective of variations in the 2DEG concentration within the top unit. This is evidenced by the consistent phase profile depicted by the red solid line in Fig. 2(e). To provide further clarity on the interrelationship between the ER and EMR transition within the Huygens metasurface, we extract the average electric field intensity and magnetic field intensity within the unit, each normalized to its respective maximum value. Figure 2(f) depicts the normalized electric field intensity (red solid line), the magnetic field intensity (blue solid line), and the ratio of the two (yellow solid line). With a gradual increase in the 2DEG concentration, the normalized electric field intensity surpasses the magnetic field intensity. At a 2DEG concentration of 10^{14} cm^{-2}, the normalized electric field intensity is 2.7 times higher than the magnetic field intensity, firmly establishing the dominance of the ER mode. This observation underscores the ability to flexibly configure the electric and magnetic field intensities by modulating the 2DEG concentration,

thereby demonstrating excellent control over the manipulation of the electromagnetic field.

C. Fabrication and Spectral Experiments

The proposed Huygens metasurface was fabricated using a standard photolithographic process, which involved multilayer lithography, electron beam lithography, and rapid thermal annealing procedures (see Section 4.C for detailed process information). The substrate utilized was a 100 µm thick SiC material, with the top and bottom units etching with IMS and SRR metal patterns, respectively. Optical microscopy images of the fabricated metasurface are provided in Figs. 3(a) and 3(b). To create nanostructured 2DEG, AlGaN/GaN heterostructures were introduced within the gaps of IMS structures. The heterostructure consisted of a 25 nm $Al_{0.27}Ga_{0.73}N$ barrier layer and a 1.5 µm GaN layer. The two ends of the heterostructure were connected to the metal through ohmic contacts to form the source and drain, while the center formed a Schottky contact, serving as an electronically controlled valve. The Huygens metasurface electrodes were attached with external PCB, as illustrated in Fig. 3(c). The voltage signal was loaded onto the gate via an SMA connector, while the sources/drains remained grounded, enabling electrically controlled adjustment of electromagnetic characteristics through carrier distribution modulation among the 2DEG nanostructures.

To measure the spectral properties of the metasurface, THz time-domain spectroscopy (THz-TDS) was employed (experimental setup provided in Section 4.D). In this experiment, broadband THz waves were emitted from a photoconductive antenna and passed through two lenses to ensure proper beam focusing on the metasurface after collimation. The electric field polarization direction was set parallel to the y-axis. During the measurement process, a gate voltage ranging from 0 to –7 V was applied to the metasurface through a DC source connected to the SMA interface on the PCB. The frequency-dependent transmission intensity spectrum was obtained by performing a fast Fourier transform of the time-domain wave detected. Figure 3(d) illustrates the transmission spectrum obtained for different gate voltages, with the bare SiC substrate serving as a reference. As the gate voltage varied from 0 to –7 V, the carrier concentration in the 2DEG within the HEMT channel experienced depletion from the saturation state. As the experimental results, the THz transmission at 321 GHz increased from 0.273 to 0.911, demonstrating a modulation efficiency of up to 90.9%. Under actual measurement conditions, the modulation efficiency exceeded 50% from 225 to 398 GHz, with a bandwidth of 173 GHz and an ROB of 56.7%, as illustrated in Fig. 3(e). The experimental results closely matched the simulation outcomes in terms of modulator transmission. Additionally, the experimental results revealed that the composite Huygens metasurface not only induced mode transition of Huygens resonance and elevated transmission but also significantly broadened the modulation bandwidth.

D. Modulation Speed Measurement

To ascertain the real-time modulation speed of the Huygens metasurface, we undertook a dynamic experiment employing a sinusoidal voltage to modulate the THz carrier wave. Within our experimental paradigm for modulated velocity
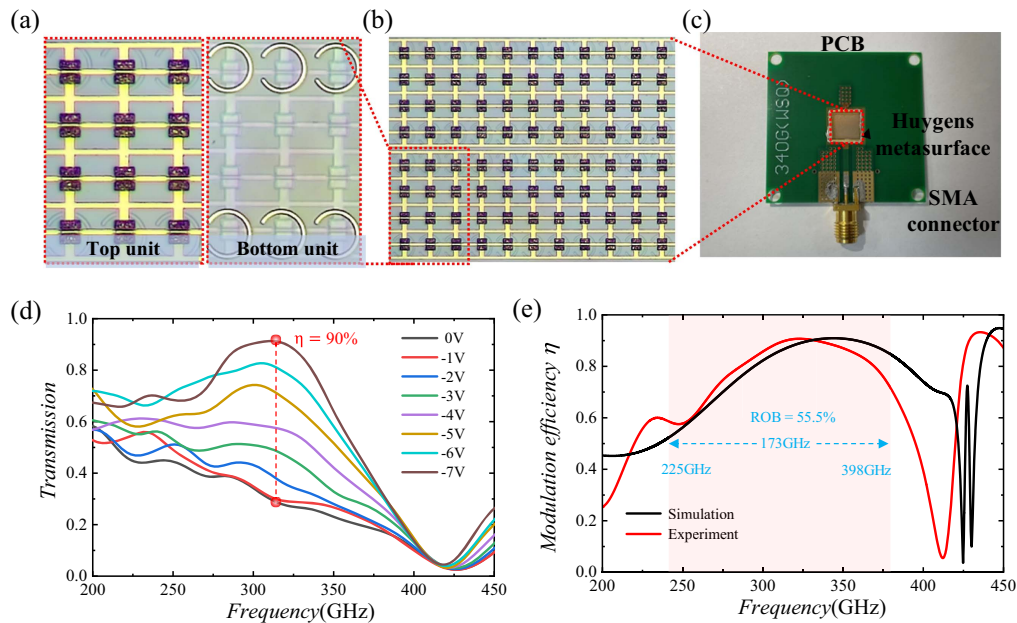
Fig. 3. Fabricated Huygens metasurface and its experimental results of spectrum characteristics. (a) Photograph of the top and bottom units. (b) Photograph of a portion of the fabricated Huygens metasurface. (c) Image of the assembled Huygens metasurface. (d) Frequency-dependent transmission curves at different gate voltages. (e) Modulation efficiency of Huygens metasurface.

analysis, we integrate three pivotal components: a terahertz wave transmitter, a terahertz wave receiver, and a modulation signal generator. The transmitter emits terahertz waves vertically irradiated onto the metasurface, enhancing the efficacy of interaction with the metasurface. Concurrently, the modulation signal generator delivers swift gate voltage to the metasurface, expediting the regulation of 2DEG depletion and saturation essential for terahertz wave propagation and truncation. This modulation technique achieves on–off keying (OOK) modulation of the terahertz wave. The OOK-modulated signal, experiencing post-normal metasurface operation, is captured by the terahertz wave receiver, culminating in a signal modulation process with efficacy (see Section 4.D for details of the measurement system). Figures 4(a) and 4(b) depict the dynamic measurement results for modulation frequencies ranging from 300 MHz to 6 GHz. All demodulated signals exhibited sinusoidal waveforms, indicating favorable modulation characteristics. The maximum continuous modulation speed corresponds to a time scale of 167 ps. Notably, as the modulated signal frequency increased gradually, the intensity of the demodulated signal diminished. This observation can be attributed to inconsistency variations in the concentration of 2DEG carriers within each HEMT present in the Huygens metasurface. These variations result in impedance mismatch between the internal and external circuits and the lossy feeding of high-frequency modulation signals into individual gates, consequently reducing the modulation efficiency and decreasing the amplitude of the demodulated signals. Despite the aforementioned challenge, our metasurface still achieves extremely high continuous modulation speed. A complete sinusoidal waveform was detected within the measured band range.

Additionally, to evaluate the carrier operating bandwidth of the metasurface, we keep the modulation frequency fixed at 1 GHz and vary the carrier frequency from 327 to 348 GHz. Figure 4(c) presents the amplitude variation of the demodulated signal at different carrier frequencies with a modulation rate of 1 GHz. The maximum demodulation intensity is obtained at a carrier frequency of 338 GHz, with a gradual decay in demodulation amplitude observed on both sides of the carrier frequency. This phenomenon can be attributed to the output bandwidth limitation of our experimental system multiplier link. Figure 4(d) shows the maximum output power of our experimental system multiplier link at 338 GHz, with the output power gradually decreasing for both end frequencies, resulting in convexity in the intensity of the received modulated signal across the carrier spectrum. This issue can be addressed by replacing the current source with a broadband THz source. Nevertheless, the Huygens metasurface has been experimentally verified to exhibit excellent modulation performance and high-speed modulation effects across a wide spectral range.

3. CONCLUSION

We have presented a novel approach for achieving ultrafast and highly efficient modulation of terahertz waves using a 2EDG Huygens metasurface. By combining an active 2DEG metasurface with a passive metasurface, we have successfully achieved dynamic conversion between ER and EMR modes through the manipulation of the carrier concentration in the 2DEG layer controlling the current phase of both layers. To demonstrate the feasibility of our proposed metasurface, we conducted comprehensive experimental measurement. Nanofabrication techniques were employed to fabricate the metasurface, and its
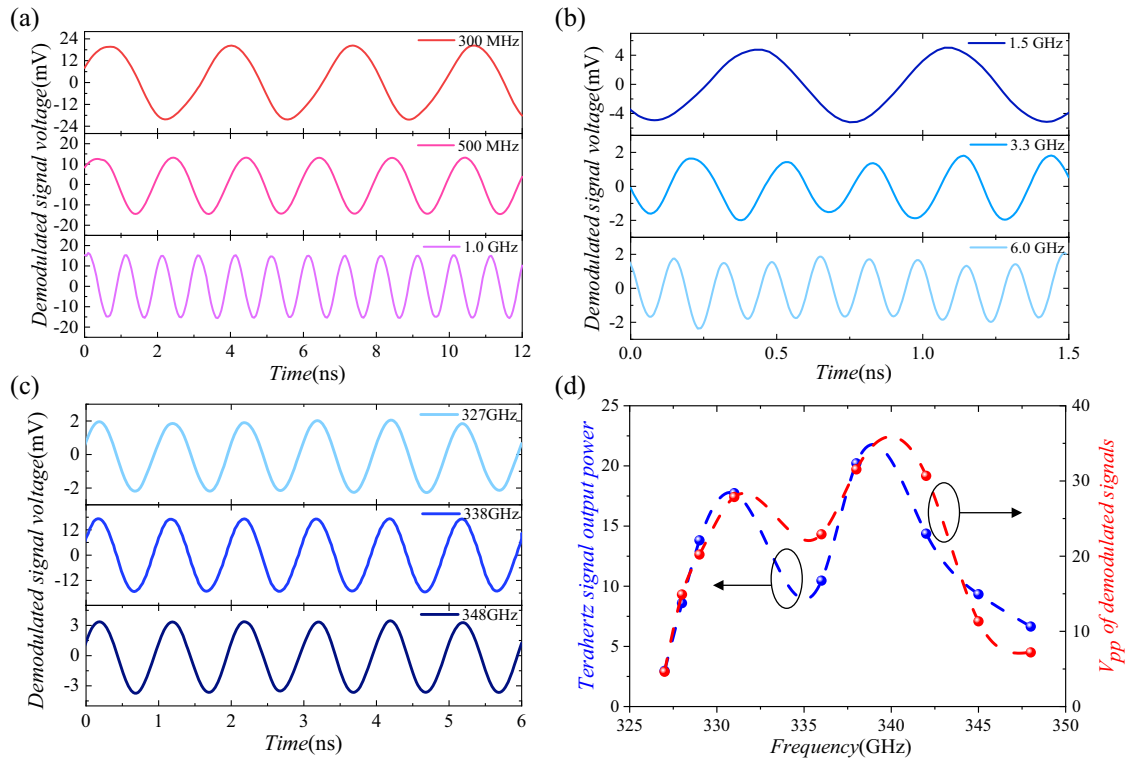
Fig. 4. Measurement results of THz Huygens metasurface modulation speed. (a), (b) Demodulated THz waveforms received by the detector. (c) Demodulated waveforms at different THz carrier frequencies with 1 GHz modulation speed. (d) Demodulated waveform amplitudes at different carrier frequencies with distinct output powers.

spectral performance was characterized using time-domain spectroscopy measurements. The dynamic modulation performance was assessed through terahertz solid-state electron system measurements. Remarkably, experimental results exhibited agreement with the numerical simulations. Our metasurface reveals remarkable achievements in modulation efficiency, with a measured efficiency of 90.9%. Furthermore, the effective bandwidth, defined as the range where the modulation efficiency remains above 50%, reaches an impressive 176 GHz. Moreover, we have demonstrated a continuous modulation speed of up to 6 GHz, surpassing the limitations of conventional microwave and optical methods in terahertz metasurface. The proposed method not only addresses the challenges of low modulation efficiency, slow modulation rates, and narrow bandwidth but also offers a platform for integrating concepts such as information coding and Snell's theorem. This integration holds the potential to unlock broad and efficient electromagnetic multifunctional manipulation capabilities. Consequently, our approach holds promising applications in high-speed wireless communication, super-resolution imaging, and efficient high-speed beam manipulation.

4. MATERIALS AND METHODS

A. Device Modeling

The metasurface was subjected to a comprehensive full-wave electromagnetic simulation using the industry-standard software CST Microwave Studio. To accurately capture the behavior of the metasurface, unit cell boundary conditions were applied to the x-axis and y-axis of the unit structure, effectively simulating the entire metasurface. Meanwhile, an open boundary was set along the z-axis to ensure accurate representation of the metasurface's response to electromagnetic waves. The polarization of the electric field was aligned along the y-direction, while the incident electromagnetic wave propagated perpendicularly to the metasurface along the z-direction. The simulation was conducted using the frequency domain solver, enabling thorough analysis of the metasurface's performance.

The intricate components comprising our metasurface are depicted in Fig. 5. This well-conceived design takes advantage of the inherent characteristics of GaN, specifically its spontaneous polarization, as well as the piezoelectric polarization within the AlGaN/GaN heterostructure. As a result, a 2DEG with an exceptionally high surface density is formed. Notably, our metasurface features an ohmic contact between the metal plate and AlGaN, while an elongated metal gate wire, positioned at the center, establishes a Schottky contact with AlGaN within the IMS gap. By precisely controlling the applied voltage, we are able to manipulate the concentration of the 2DEG, thereby adjusting both the thickness of the depletion layer beneath the Schottky contact and the height of the Schottky barrier to suit our specific requirements.

During the simulation process, the 2DEG within the metasurface is partitioned into two distinct regions, as depicted in Fig. 5(d). The first region corresponds to the 2DEG gated active area, which interfaces with the gate line. It exhibits a
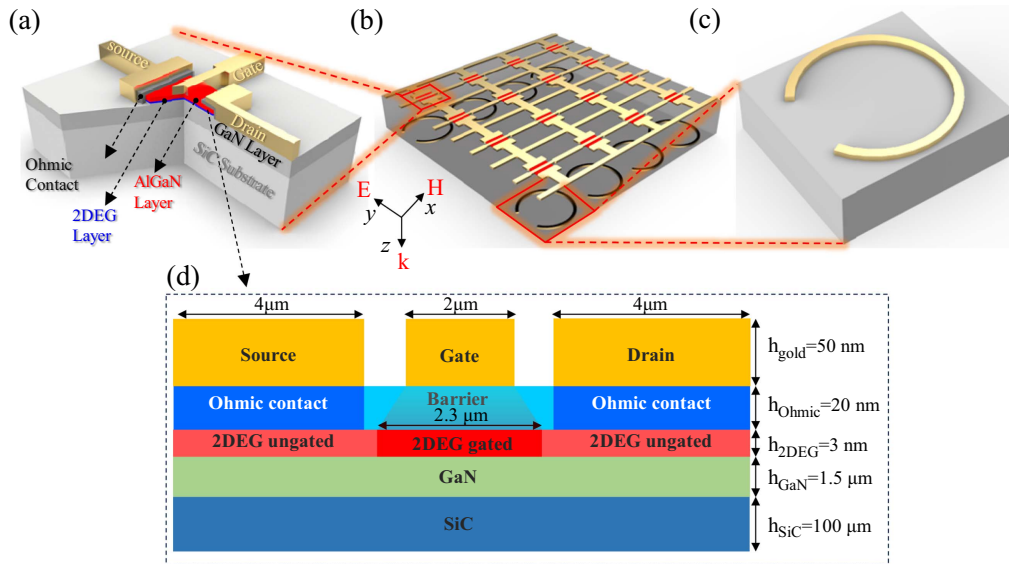
Fig. 5. Schematic of the device we designed. (a) Composition of the HEMT region of the top unit. (b) Model diagram of the 4 × 1 arrays. (c) SRR in the bottom unit. (d) Cross section and dimension label of the HEMT in the *yoz*-plane and size label of the HEMT.

varying electron concentration in response to changes in the gate voltage and spans a width 0.3 μm wider than the gate line itself [57]. The second region refers to the 2DEG ungated active region, which forms an ohmic contact with the source and drain electrodes. In this region, the electron concentration remains constant relative to the gate voltage.

An AlGaN layer with a dielectric constant of 10 is established between the gate and the 2DEG gated region to simulate the Schottky contact of the gate. A conductive layer with a conductivity of 2427 S/m is established between the source, drain, and 2DEG ungated to simulate and characterize the ohmic contact [57]. Following the 2DEG thin layer is a GaN layer with a dielectric constant of 9.8 and a thickness of about 1.5 μm. The overall structural system of AlGaN/GaN high-electron-mobility transistor (HEMT) is placed on a 100 μm SiC substrate.

During room temperature operation, the carrier concentration of the 2DEG is measured at approximately 1.125×10^{11} cm^{-2}, while the electron mobility reaches up to 2248 cm^2/(V · s). The square resistance of the device amounts to 250 Ω. These parameters collectively contribute to the excellent performance demonstrated in our experimental results.

In this study, the Drude model [56,63] implemented within CST Microwave Studio is utilized to analyze the transport characteristics of the 2DEG in GaN HEMTs. The change in carrier concentration is simulated by altering the plasma frequency in the model. To simulate the varying physical characteristics of the 2DEG under different voltages, its equivalent complex dielectric constant is expressed as follows:

$$\varepsilon(\omega) = \varepsilon_\infty + j\omega_p^2 \frac{\gamma\omega^{-1}}{\omega^2 + \gamma^2}. \tag{1}$$

Here, ε_∞ represents the real part of the complex permittivity, with a magnitude of $9.8\varepsilon_0$, which is equivalent to the permittivity of GaN. The imaginary part of the complex dielectric

constant is described by the Drude model, where ω_p denotes the plasma frequency and γ represents the electron collision frequency.

The plasma frequency is specifically expressed as

$$\omega_p^2 = \frac{e^2 N_s}{\varepsilon_0 m^* d}. \tag{2}$$

The electron collision frequency is specifically expressed as

$$\gamma = \frac{e}{m^* \mu}. \tag{3}$$

In these equations, m^* represents the effective mass of electrons in the 2DEG, d denotes the thickness of the 2DEG channel, N_s corresponds to the carrier surface density of the 2DEG, e represents the charge of an electron, and μ represents the electron mobility of the 2DEG. During simulation, manipulating the plasma frequency within the Drude model enables the simulation of equivalent carrier density changes.

B. Average Surface Impedance of Huygens Metasurface

Huygens metasurfaces are characterized by the surface electric admittance and surface magneto-impedance, which can be manipulated to generate arbitrary electromagnetic fields in specific regions. This capability allows for the independent specification of field distributions in space. The surface current density $\vec{J}_s$ and magnetic current density $\vec{M}_s$ are the corresponding quantities associated with these fields, as given by Eqs. (4) and (5), respectively:

$$\vec{J}_s = \hat{n} \times (\vec{H}_2 - \vec{H}_1), \tag{4}$$

$$\vec{M}_s = -\hat{n} \times (\vec{E}_2 - \vec{E}_1). \tag{5}$$

To describe the electromagnetic properties of the metasurface, we establish a relationship between the average tangential electric field $\vec{E}_{t,\text{avg}}$ and magnetic field $\vec{H}_{t,\text{avg}}$ at the desired

boundary and the desired current density, expressed by Eqs. (6) and (7), respectively:

$$\vec{E}_{t,\text{avg}} = \overline{\overline{Z}}_{\text{MS}} \cdot \vec{J}_s, \tag{6}$$

$$\vec{H}_{t,\text{avg}} = \overline{\overline{Y}}_{\text{ES}} \cdot \vec{M}_s. \tag{7}$$

In this particular design, the incident wave field is a linearly polarized wave that propagates without polarization conversion. As a consequence, the spatially varying surface conductance $\overline{\overline{Y}}_{\text{ES}}$ and magnetic impedance $\overline{\overline{Z}}_{\text{MS}}$ can be simplified as scalars. By combining the aforementioned equations, the field at the discontinuous section with the electrical admittance and magneto-impedance of the metasurface can be obtained, as described by Eqs. (8) and (9), respectively:

$$\vec{E}_{t,\text{avg}} = \overline{\overline{Z}}_{\text{MS}} \cdot (\hat{n} \times (\vec{H}_2 - \vec{H}_1)), \tag{8}$$

$$\vec{H}_{t,\text{avg}} = \overline{\overline{Y}}_{\text{ES}} \cdot (-\hat{n} \times (\vec{E}_2 - \vec{E}_1)). \tag{9}$$

The normalized surface electric admittance $Y_{\text{ES}} \cdot \eta$ and surface magneto-impedance Z_{MS}/η can be obtained from the transmission coefficient t and the reflection coefficient r:

$$Z^e_{\text{MS}} = \frac{Z_{\text{MS}}}{\eta} = \frac{2(1 - t + r)}{1 + t - r}, \tag{10}$$

$$Y^e_{\text{ES}} = Y_{\text{ES}} \cdot \eta = \frac{2(1 - t - r)}{1 + t + r}, \tag{11}$$

where $\eta = \sqrt{\mu/\varepsilon}$ is the wave impedance of free space. According to Huygens' principle, when the surface conductivity and magnetic impedance of a metasurface are purely imaginary and equal, the effect of perfect transmission is produced and lossless properties are exhibited.

Based on our calculations and analysis conducted in accordance with the Huygens principle, we have generated plots depicting the surface electric admittance and surface magneto-impedance characteristics. The results, presented in Fig. 6, reveal intriguing behaviors of the Huygens metasurface under varying conditions. For low concentrations of the two-dimensional electron gas (2DEG), both the real parts of the surface magneto-impedance and surface electrical admittance are observed to be zero. Furthermore, their imaginary parts converge at 333 GHz. At this specific point, the Huygens metasurface exhibits a state of low loss, which is of great significance. As we increase the concentration of the 2DEG within the operating frequency range, notable changes in the metasurface behavior are observed. Specifically, the real part of the surface magneto-impedance continues to rise, leading to a reduction in the intensity of the magnetic field. Conversely, the real part of the surface electrical admittance remains nearly constant, hovering around zero, showcasing typical electrical resonance characteristics. Consequently, the Huygens metasurface undergoes a transition from Huygens resonance to a single electrical resonance mode. These findings shed light on the dynamic nature of the Huygens metasurface, highlighting the influence of the 2DEG concentration on its resonance properties. Such insights contribute to our understanding of the underlying mechanisms
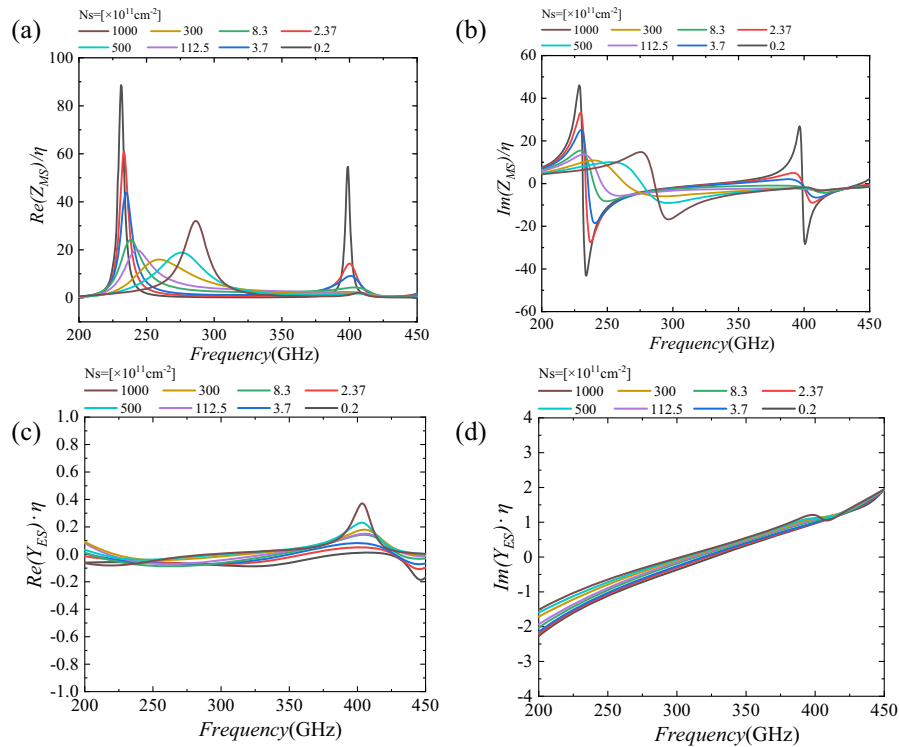

Fig. 6. Z_{MS} and Y_{ES} of the THz modulator vary with incident wave frequency at different carrier concentrations. (a) Calculation results of the real part of Z_{MS}. (b) Calculation results of the imaginary part of Z_{MS}. (c) Calculation results of the real part of Y_{ES}. (d) Calculation results of the imaginary part of Y_{ES}.

governing the performance of these metasurfaces and open avenues for further exploration and optimization in future applications.

C. Device Processing and Assembly

The fabrication process of the Huygens metasurface chip involves a meticulously orchestrated sequence of six key steps. Initially, an AlGaN heterostructure thin film is deposited onto a SiC substrate employing a chemical deposition method. The active area of the high-electron-mobility transistor (HEMT) is then defined by photolithography with the aid of a mask. Subsequently, the AlGaN thin film undergoes a plasma treatment using a Cl_2–BCl_3 mixture, followed by an etching process that shapes the HEMT's active meta structure. A composite metal layer comprising titanium, aluminum, nickel, and gold is then precisely deposited onto the active mesa, serving as the source and drain electrodes of the HEMT. This intricate metal deposition is achieved through photolithography, electron beam evaporation, and lift-off processes. To form ohmic contacts, the source-drain electrodes undergo rapid thermal annealing in a helium environment. Furthermore, a metal structure is deposited onto the GaN thin film using the same series of photolithography, electron beam evaporation, and lift-off processes. Following this, the IMS pattern structure is fabricated on the top side, while the SRR pattern is fabricated on the back side using identical methods. To safeguard the integrity of the processed chip and prevent oxidation of the metal structure, a SiN passivation film is meticulously applied to its surface, ensuring the protection of the Huygens metasurface.

For convenient power feeding and testing, the processed Huygens metasurface is assembled onto a PCB featuring a central hollow. Conductive adhesive is employed to secure the metasurface onto the board, enabling reliable electrical connections. The PCB incorporates a dedicated circuit that is electrically linked to the electrodes on the chip using delicate bonding wires. To facilitate signal input into the HEMT array within the chip, an SMA connector is connected to the circuit on the PCB. Through this well-constructed setup, the modulated signal can be efficiently channeled into the HEMT array, unleashing the potential of the Huygens metasurface.

D. Experimental System

As illustrated in Fig. 7, our spectrum characteristics experimental setup involves the implementation of a femtosecond laser pulse, which is divided into two beams using a fiber splitter. One beam acts as the transmitter, responsible for exciting the pulse, while the other beam serves as the probe pulse. The probe pulse traverses a time delay line before reaching the photoconductive antenna (PCA), where it serves as the receiver. The transmitter beam, emitting a spherical wave in the y-polarization direction, passes through the PCA and undergoes collimation into a plane wave using lens 1. This plane wave is subsequently focused onto the test array with the aid of lens 2. Upon passing through the array, the THz waves are converted back into plane waves using lens 3. Finally, lens 4 refocuses these plane waves onto the receiver's PCA. To ensure precise control over the metasurface in our test system, a DC source is employed for feeding purposes. The feeding voltage can be adjusted within the range of 0 to –7 V, allowing for exploration of the spectrum characteristics.

In our modulation speed experimental setup, as illustrated in Fig. 8, we have designed a dynamic system comprising three essential components: a terahertz wave transmitter, a terahertz wave receiver, and a modulated signal generator. The terahertz wave transmitter involves a precise oscillator module, a terahertz frequency multiplier link, and a horn antenna. By feeding a local oscillator signal ranging from 13.5 to 14.75 GHz from the RF signal source (Agilent E8257D) into the 24-frequency link, we generate terahertz waves spanning from 324 to 354 GHz, with a maximum output power of 20 mW at 338 GHz. These terahertz waves are then emitted into free space in a direction through a 25 dB terahertz standard horn antenna, precisely targeted at the Huygens metasurface. To drive the modulation function on the terahertz waves, we employ a modulated signal generator. This generator comprises a continuous sinusoidal signal transmitter (Ceyear 1465L), a bias junction, and a DC circuit. The bias junction and DC circuit
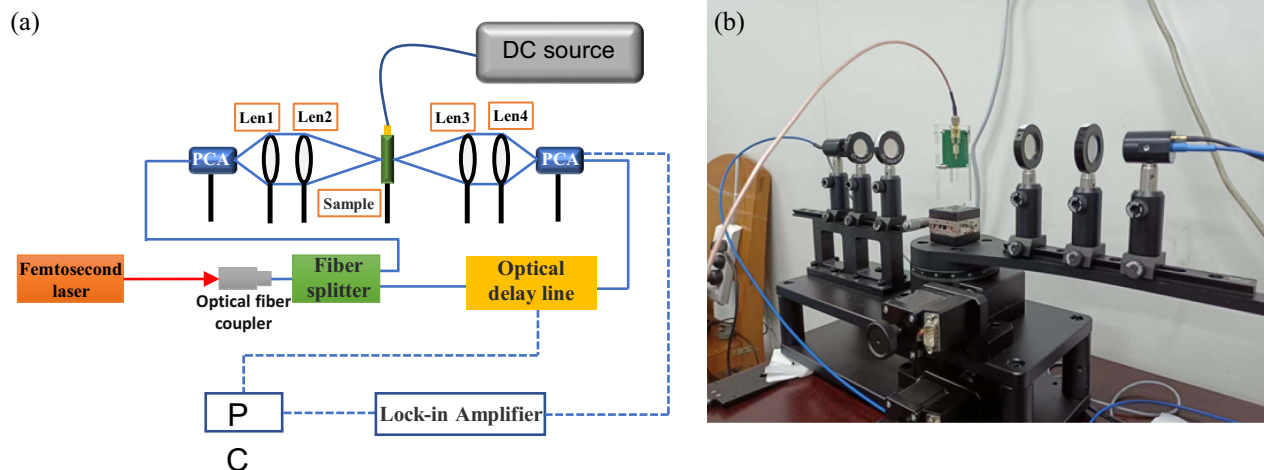

Fig. 7.   THz-TDS experimental system. (a) Schematic and (b) photo of the test system.
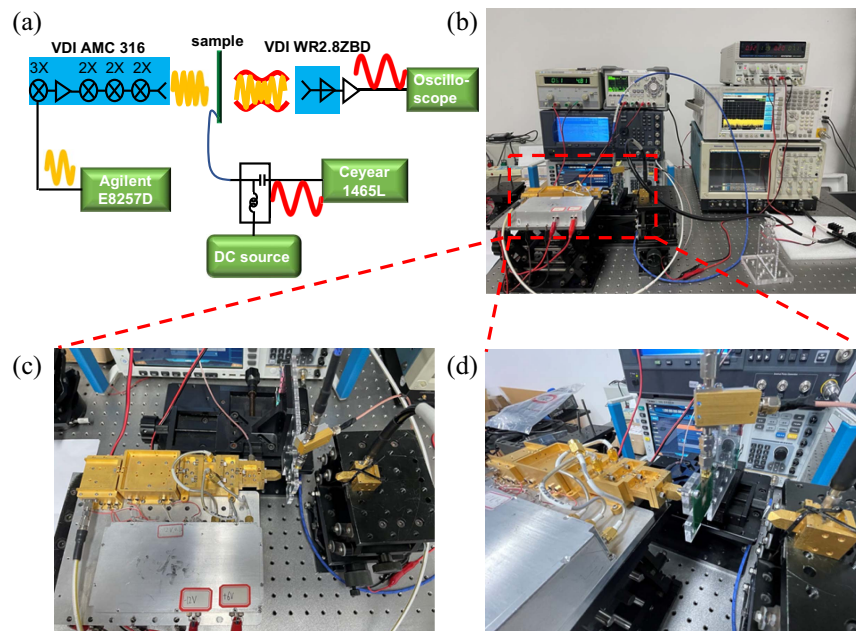
Fig. 8. Dynamic experimental system. (a) Schematic of the system. (b) Photo of the system. (c), (d) Partial detail drawings of the system.

are incorporated to optimize the operation of the HEMT, ensuring that the high and low levels of the continuous sinusoidal signal effectively control the depletion and saturation of the 2DEG. The modulated signal obtained after the proper operation of the metasurface, driven by the modulated signal generator, is captured by a 25 dB terahertz standard horn antenna positioned on the terahertz wave receiver. To analyze the captured signal, we utilize a terahertz detector (VDI WR2.8ZBD) positioned behind the antenna. This detector allows us to accurately measure the envelope of the modulated terahertz signal. The demodulated waveform is further observed and analyzed using an oscilloscope (Tektronix TDS6604B).

Author Contributions. Xuan Cong and Hongxin Zeng conceived the idea of the ultrafast modulable 2DEG Huygens metasurface. Shiqi Wang and Sen Gong carried out device assembly and constructed the experiment environment. Shixiong Liang and Feng Zhihong provided the production and preparation of the 2DEG metasurface. Lan Wang and Huajie Liang helped with the simulation. Lin Huang and Feng Lan performed experiments. Zheng Wang, Weipeng Wang, and Haoyi Cao performed the data analyses. Ziqiang Yang participated in the discussion of potential setups for the tests/measurements, and helped to draft the paper.

Yaxin Zhang and Tie Jun Cui contributed substantially to providing theoretical guidance.

REFERENCES

1. S. Sun, Q. He, J. Hao, *et al.*, "Electromagnetic metasurfaces: physics and applications," Adv. Opt. Photon. **11**, 380–479 (2019).
2. A. Nemati, Q. Wang, M. Hong, *et al.*, "Tunable and reconfigurable metasurfaces and metadevices," Opto-Electron. Adv. **1**, 18000901 (2018).
3. F. Ding, Y. Yang, R. A. Deshpande, *et al.*, "A review of gap-surface plasmon metasurfaces: fundamentals and applications," Nanophotonics **7**, 1129–1156 (2018).
4. Y. Yang, Y. Bi, L. Peng, *et al.*, "Veselago lensing with Weyl metamaterials," Optica **8**, 249–254 (2021).
5. X. Cong, L. Zhang, J. Li, *et al.*, "Integration of ultrathin metasurfaces with a lens for efficient polarization division multiplexing," Adv. Opt. Mater. **7**, 1900116 (2019).
6. L. Li, P. Zhang, F. Cheng, *et al.*, "An optically transparent near-field focusing metasurface," IEEE Trans. Microwave Theory Techn. **69**, 2015–2027 (2021).
7. M. Khorasaninejad, W. T. Chen, R. C. Devlin, *et al.*, "Metalenses at visible wavelengths: diffraction-limited focusing and subwavelength resolution imaging," Science **352**, 1190–1194 (2016).
8. H. Ma, J. Niu, B. Gao, *et al.*, "Tunable metasurface based on plasmonic quasi bound state in the continuum driven by metallic quantum wells," Adv. Opt. Mater. **11**, 2202584 (2023).
9. M. Chang, J. Han, Y. Li, *et al.*, "Self-powered polarization-reconfigurable rectenna for wireless power transfer system," IEEE Trans. Antennas Propag. **71**, 6297–6307 (2023).
10. P. Xu, H. Liu, R. Li, *et al.*, "Highly integrated multifunctional coding metasurface in full-space based on independent control of transmission and reflection," Adv. Opt. Mater. **12**, 2203117 (2023).

11. N. Yu, P. Genevet, M. A. Kats, *et al.*, "Light propagation with phase discontinuities: generalized laws of reflection and refraction," Science **334**, 333–337 (2011).

12. Z. Qin, Y. Li, H. Wang, *et al.*, "Polarization meta-converter for dynamic polarization states shifting with broadband characteristic," Opt. Express **30**, 20014–20025 (2022).

13. K. Liu, G. Wang, T. Cai, *et al.*, "Dual-band transmissive circular polarization generator with high angular stability," Opt. Express **28**, 14995–15005 (2020).

14. X. Huang, H. Yang, D. Zhang, *et al.*, "Ultrathin dual-band metasurface polarization converter," IEEE Trans. Antennas Propag. **67**, 4636–4641 (2019).

15. X. G. Zhang, W. X. Jiang, H. L. Jiang, *et al.*, "An optically driven digital metasurface for programming electromagnetic functions," Nat. Electron. **3**, 165–171 (2020).

16. Y. Che, X. Wang, Q. Song, *et al.*, "Tunable optical metasurfaces enabled by multiple modulation mechanisms," Nanophotonics **9**, 4407–4431 (2020).

17. L. Wang, Y. Zhang, X. Guo, *et al.*, "A review of THz modulators with dynamic tunable metasurfaces," Nanomaterials **9**, 965 (2019).

18. J. Wang, B. Xiong, R. Peng, *et al.*, "Flexible phase change materials for electrically-tuned active absorbers," Small **17**, 2101282 (2021).

19. Y. Li, J. Lin, H. Guo, *et al.*, "A tunable metasurface with switchable functionalities: from perfect transparency to perfect absorption," Adv. Opt. Mater. **8**, 1901548 (2020).

20. Y. Liu, R. Zhong, J. Huang, *et al.*, "Independently tunable multi-band and ultra-wide-band absorbers based on multilayer metal-graphene metamaterials," Opt. Express **27**, 7393–7404 (2019).

21. A. Pitilakis, O. Tsilipakos, F. Liu, *et al.*, "A multi-functional reconfigurable metasurface: electromagnetic design accounting for fabrication aspects," IEEE Trans. Antennas Propag. **69**, 1440–1454 (2021).

22. C. Molero, A. Palomares-Caballero, A. Alex-Amor, *et al.*, "Metamaterial-based reconfigurable intelligent surface: 3D meta-atoms controlled by graphene structures," IEEE Commun. Mag. **59**, 42–48 (2021).

23. W. Tang, J. Y. Dai, M. Z. Chen, *et al.*, "MIMO transmission through reconfigurable intelligent surface: system design, analysis, and implementation," IEEE J. Sel. Areas Commun. **38**, 2683–2699 (2020).

24. F. Liu, O. Tsilipakos, A. Pitilakis, *et al.*, "Intelligent metasurfaces with continuously tunable local surface impedance for multiple reconfigurable functions," Phys. Rev. Appl. **11**, 044024 (2019).

25. A. Forouzmand and H. Mosallaei, "A tunable semiconductor-based transmissive metasurface: dynamic phase control with high transmission level," Laser Photon. Rev. **14**, 1900353 (2020).

26. A. Forouzmand, M. M. Salary, G. Kafaie Shirmanesh, *et al.*, "Tunable all-dielectric metasurface for phase modulation of the reflected and transmitted light via permittivity tuning of indium tin oxide," Nanophotonics **8**, 415–427 (2019).

27. Y. Zhang, Y. Zhao, S. Liang, *et al.*, "Large phase modulation of THz wave via an enhanced resonant active HEMT metasurface," Nanophotonics **8**, 153–170 (2018).

28. B. Dong, C. Zhang, G. Guo, *et al.*, "BST-silicon hybrid terahertz meta-modulator for dual-stimuli-triggered opposite transmission amplitude control," Nanophotonics **11**, 2075–2083 (2022).

29. L. Ye, X. Chen, C. Zhu, *et al.*, "Switchable broadband terahertz spatial modulators based on patterned graphene and vanadium dioxide," Opt. Express **28**, 33948–33958 (2020).

30. J. Lou, J. Liang, Y. Yu, *et al.*, "Silicon-based terahertz meta-devices for electrical modulation of Fano resonance and transmission amplitude," Adv. Opt. Mater. **8**, 2000449 (2020).

31. S. Wei, G. Cao, H. Lin, *et al.*, "A varifocal graphene metalens for broadband zoom imaging covering the entire visible region," ACS Nano **15**, 4769–4776 (2021).

32. G. K. Shirmanesh, R. Sokhoyan, P. C. Wu, *et al.*, "Electro-optically tunable multifunctional metasurfaces," ACS Nano **14**, 6912–6920 (2020).

33. E. Klopfer, M. Lawrence, D. R. Barton, *et al.*, "Dynamic focusing with high-quality-factor metalenses," Nano Lett. **20**, 5127–5132 (2020).

34. J. Y. Dai, J. Yang, W. Tang, *et al.*, "Arbitrary manipulations of dual harmonics and their wave behaviors based on space-time-coding digital metasurface," Appl. Phys. Rev. **7**, 041408 (2020).

35. J. Y. Dai, W. Tang, M. Wang, *et al.*, "Simultaneous in situ direction finding and field manipulation based on space-time-coding digital metasurface," IEEE Trans. Antennas Propag. **70**, 4774–4783 (2022).

36. J. Y. Dai, L. X. Yang, J. C. Ke, *et al.*, "High-efficiency synthesizer for spatial waves based on space-time-coding digital metasurface," Laser Photon. Rev. **14**, 1900133 (2020).

37. X. Zhu, C. Qian, Y. Jia, *et al.*, "Realization of index modulation with intelligent spatiotemporal metasurfaces," Adv. Intell. Syst. **5**, 2300065 (2023).

38. Q. Yang, S. Kruk, Y. Xu, *et al.*, "Mie-resonant membrane Huygens' metasurfaces," Adv. Funct. Mater. **30**, 1906851 (2020).

39. R. Zhao, Z. Zhu, G. Dong, *et al.*, "High-efficiency Huygens' metasurface for terahertz wave manipulation," Opt. Lett. **44**, 3482–3485 (2019).

40. C. Guan, Z. Wang, X. Ding, *et al.*, "Coding Huygens' metasurface for enhanced quality holographic imaging," Opt. Express **27**, 7108–7119 (2019).

41. V. Popov, B. Ratni, S. N. Burokur, *et al.*, "Non-local reconfigurable sparse metasurface: efficient near-field and far-field wavefront manipulations," Adv. Opt. Mater. **9**, 2001316 (2021).

42. K. Chen, Y. Feng, F. Monticone, *et al.*, "A reconfigurable active Huygens' metalens," Adv. Mater. **29**, 1606422 (2017).

43. J. Wu, F. Tang, J. Ma, *et al.*, "Angle-sensitive dynamic optical modulation based on Huygens metasurfaces," Results Phys. **18**, 103226 (2020).

44. M. M. Salary and H. Mosallaei, "Tunable all-dielectric metasurfaces for phase-only modulation of transmitted light based on quasi-bound states in the continuum," ACS Photon. **7**, 1813–1829 (2020).

45. A. Leitis, A. Heßler, S. Wahl, *et al.*, "All-dielectric programmable Huygens' metasurfaces," Adv. Funct. Mater. **30**, 1910259 (2020).

46. K. Fan, I. V. Shadrivov, and W. J. Padilla, "Dynamic bound states in the continuum," Optica **6**, 169–173 (2019).

47. A. Komar, R. Paniagua-Domínguez, A. Miroshnichenko, *et al.*, "Dynamic beam switching by liquid crystal tunable dielectric metasurfaces," ACS Photon. **5**, 1742–1748 (2018).

48. Q. Zhou, Q. Qiu, T. Wu, *et al.*, "Ultrafast all-optical switching modulation of terahertz polarization conversion metasurfaces based on silicon," ACS Omega **8**, 48465–48479 (2023).

49. A. Tognazzi, P. Franceschini, O. Sergaeva, *et al.*, "Giant photoinduced reflectivity modulation of nonlocal resonances in silicon metasurfaces," Adv. Photon. **5**, 066006 (2023).

50. A. Howes, Z. Zhu, D. Curie, *et al.*, "Optical limiting based on Huygens' metasurfaces," Nano Lett. **20**, 4638–4644 (2020).

51. T. Kang, Z. Ma, J. Qin, *et al.*, "Large-scale, power-efficient Au/VO$_2$ active metasurfaces for ultrafast optical modulation," Nanophotonics **10**, 909–918 (2020).

52. M. R. Shcherbakov, S. Liu, V. V. Zubyuk, *et al.*, "Ultrafast all-optical tuning of direct-gap semiconductor metasurfaces," Nat. Commun. **8**, 17 (2017).

53. A. Tognazzi, M. Gandolfi, B. Li, *et al.*, "Opto-thermal dynamics of thin-film optical limiters based on the VO$_2$ phase transition," Opt. Mater. Express **13**, 41–52 (2023).

54. Q. Zhou, T. Wu, Y. Li, *et al.*, "Multifunctional metasurface for ultrafast all-optical efficient modulation of terahertz wave," Opt. Commun. **555**, 130244 (2024).

55. K.-S. Im, J.-B. Ha, K.-W. Kim, *et al.*, "Normally off GaN MOSFET based on AlGaN/GaN heterostructure with extremely high 2DEG density grown on silicon substrate," IEEE Electron Device Lett. **31**, 192–194 (2010).

56. Y. Zhang, S. Qiao, S. Liang, *et al.*, "Gbps terahertz external modulator based on a composite metamaterial with a double-channel heterostructure," Nano Lett. **15**, 3501–3506 (2015).

57. Y. Zhao, L. Wang, Y. Zhang, *et al.*, "High-speed efficient terahertz modulation based on tunable collective-individual state conversion within an active 3 nm two-dimensional electron gas metasurface," Nano Lett. **19**, 7588–7597 (2019).

58. F. Lan, L. Wang, H. Zeng, *et al.*, "Real-time programmable metasurface for terahertz multifunctional wave front engineering," Light Sci. Appl. **12**, 191 (2023).

59. C. Pfeiffer and A. Grbic, "Metamaterial Huygens' surfaces: tailoring wave fronts with reflectionless sheets," Phys. Rev. Lett. **110**, 197401 (2013).

60. A. Rahimzadegan, D. Arslan, D. Dams, *et al.*, "Beyond dipolar Huygens' metasurfaces for full-phase coverage and unity transmittance," Nanophotonics **9**, 75–82 (2019).

61. A. Howes, W. Wang, I. Kravchenko, *et al.*, "Dynamic transmission control based on all-dielectric Huygens metasurfaces," Optica **5**, 787–792 (2018).

62. M. Liu, D. A. Powell, Y. Zarate, *et al.*, "Huygens' metadevices for parametric waves," Phys. Rev. X **8**, 031077 (2018).

63. D. Shrekenhamer, S. Rout, A. C. Strikwerda, *et al.*, "High speed terahertz modulation from metamaterials with embedded high electron mobility transistors," Opt. Express **19**, 9968–9975 (2011).